Supporting Information

High-yield electrochemical hydrogen peroxide production from an enhanced two-electron oxygen reduction pathway by mesoporous nitrogen-doped carbon and manganese hybrid electrocatalysts

Ayeong Byeon,[a,b] Jinwon Cho,[a] Jong Min Kim,[c] Keun Hwa Chae,[d] Hee-Young Park,[a] Seok Won Hong,[e] Hyung Chul Ham,[f] Seung Woo Lee,[g] Ki Ro Yoon,[h] and Jin Young Kim[a]**

[a]Fuel Cell Research Center, Korea Institute of Science and Technology (KIST), Hwarangno 14-gil 5, Seongbuk-gu, Seoul, 02792, Republic of Korea

[b]Advanced Materials R&D, LG Chemical Research Park, 188 Munji-ro, Yuseong-gu, Daejeon 34122, Republic of Korea

[c]Materials Architecturing Research Center, Korea Institute of Science and Technology, Hwarangno 14-gil 5, Seongbuk-gu, Seoul 02792, Republic of Korea

[d]Advanced Analysis Center, Korea Institute of Science and Technology (KIST), Hwarangno 14-gil 5, Seongbuk-gu, Seoul, 02792, Republic of Korea

[e]Water Cycle Research Center, KIST, Seoul 02792, Republic of Korea

[f]Chemical Engineering, Inha University, Incheon, 22212, Republic of Korea

[g]G. W. Woodruff School of Mechanical Engineering, Georgia Institute of Technology, Atlanta, GA 30332, USA

[h]Technical Textile and Materials R&D Group, Korea Institute of Industrial Technology (KITECH), 143, Hanggaul-ro, Sangnok-gu, Ansan-si, Gyeonggi-do, 15588, Republic of Korea

**E-mail: kryoon@kitech.re.kr (K. R. Y) and jinykim@kist.re.kr (J. Y. K)*

Preparation of N-doped carbon spheres (NCs)

3.14 g of ammonium persulfate ($(NH4)_2SO_4$; APS, Sigma-Aldrich) and 40 ml of various-sized (5, 12, and 20 nm) colloidal silica (Ludox HS-40, 40 wt%; Sigma-Aldrich) were mixed with 100 ml of 5 mM formic acid solution (Sigma-Aldrich). The temperature was maintained at 2 °C and 2 ml of aniline (Sigma-Aldrich) was added to the solution under vigorous stirring. The polymerization was conducted for 24 h at 2 °C. After that, the dark greenish solution was washed several times in deionized (DI) water until the pH value reached 6–7, then dried at 60 °C overnight. The residue was collected, followed by heat treatment at 800 °C for 2 h (ramping rate: 5 °C/min) under an Ar atmosphere. To remove silica nanoparticles embedded in the resulting carbon material, 1 M NaOH solution was added for 24 h and then washed with DI water until the pH value reached to 6–7.

Preparation of Mn-O/N@NCs

The obtained NCs were impregnated in manganese(II) acetate tetrahydrate ($(CH_3COO)_2Mn{\cdot}4H_2O$; Sigma-Aldrich)-dissolved solution at a relative mass ratio of 5–70 ($(CH_3COO)_2Mn{\cdot}4H_2O$ to NCs) in 30 ml of isopropyl alcohol (IPA; B&J Purified Plus). The solution was sonicated for 30 min, and stirred and heated to 80 °C to evaporate IPA. The manganese acetate and NC composites were heat-treated at 800 °C for 2 h with a ramping rate of 5 °C/min under Ar. The resulting material was called Mn-O/N@NCs-x (where x is the relative mass ratio of the manganese precursor to NCs).

Electrochemical half-cell measurements

An AutoLab PGSTAT20 potentiostat (Metrohm; AutoLab BV) was used for all electrochemical measurements. The catalyst ink was prepared by mixing 5 mg of catalyst, 50 μl of 5 wt. % Nafion solution (Sigma-Aldrich), and 500 μL of IPA. Then, 15 μL of the solution was deposited on the surface of a rotating ring disk electrode (RRDE; AFE7R9GCPT; Pine Research) 5.61 mm in

diameter surrounded by a Pt ring (6.25 mm inner diameter and 7.92 mm outer diameter), which was used as a working electrode. The disk and ring area were 0.2475 cm^2 and 0.1886 cm^2, respectively. The Pt wire and saturated calomel electrode (SCE) filled with saturated KCl were used as counter and reference electrodes, respectively. The measured potentials were converted to the reversible hydrogen electrode (RHE) potential based on the conversion equation, $E_{RHE} = E_{SCE} + E_{SCE}^0 + 0.059pH$ ($E_{SCE}^0 = +0.241$ V). The RRDE test was conducted by applying 1.2 V_{RHE} to the ring electrode at a rotation rate of 900 rpm, in oxygen gas (O_2)-purged 0.1 M $HClO_4$. The electron transfer number (n) and hydrogen peroxide yield (% H_2O_2) were determined as follows:

$$n = 4I_D/(I_D + (I_R/N)) \quad (1)$$

$$\% H_2O_2 = 200(I_R/N)/(I_D+(I_R/N)) \quad (2)$$

where I_D and I_R are the disk current and ring current, respectively, and N is the collection efficiency. This value was obtained by subtraction of the current measured under Ar, to remove the capacitance effect. The collection efficiency was 0.37, which we determined based on the relative ratio of the disk current and ring current from hexacyanoferrate(III) reduction ($1e^-$ reaction), for different rotation rates under Ar in an electrolyte of 0.1 M $HClO_4$ and 0.01 M hexacyanoferrate(III). This value is consistent with the manufacturer's value (0.37). An accelerated degradation test (ADT) was conducted in a potential range of 0.6–1.1 V_{RHE} in O_2-saturated 0.1 M $HClO_4$ electrolyte, at a scan rate of 50 mV/s for 1,000 cycles.

Electrochemical single-cell measurements

The MEA was fabricated by spraying ink slurry into a Nafion® 211 membrane with Pt contents of 0.2 mg/cm^2 for the Pt/C anode and 1 mg/cm^2 for the cathode. The slurry was obtained by mixing 46.7 wt% Pt/C, and the synthesized Mn-based catalyst with 5 % Nafion® solution was dispersed in IPA solution. The optimized ionomer/catalyst weight ratio was 0.273 and 0.5 for Pt/C and Mn-O/N@NCs-50-acid catalysts, respectively. The I-V curve of the prepared MEA was tested with an active area of 1 cm^2, with graphite flow field plates and gas diffusion layers (GDLs; Sigracet® 39BC). The cell temperature was set to 80 °C, and pre-humidified H_2 and O_2 gas (fully humidified gas) with flow rates of 200 and 600 ml/min, respectively, were used at a pressure of 1.8 bar. Quantitative measurement of H_2O_2 was carried out using the Dess-Martin periodinane (DMP) method and spectrophotometric measurements.

Characterizations

The morphology of the synthesized material was characterized using scanning electron microscopy (SEM; Nova200; FEI) and high-resolution transmission electron microscopy (HR-TEM; Titan and Talos; FEI). Energy dispersive spectroscopy (EDS) mapping was carried out using the Talos microscope equipped with an extreme-field emission gun (X-FEG) and super-X EDS system with four silicon drift detectors (SDDs). We evaluated the diffraction pattern and characterized the surface using X-ray diffraction (XRD; Mini Flex II; Rigaku), with a 2θ range of 10–80°, scan rate of 3°/min, and step size of 0.02°. Cu Kα radiation was used and a MultiLab 2000 (Thermo) X-ray photoelectron spectroscopy (XPS) system with Al Kα radiation (hν = 1,486.6 eV) was employed as a probe. Thermogravimetric analysis (TGA) was conducted on a TGA Q50 V20.13 Build 39 (TA Instruments) with a temperature range of 20–900 °C and a heating rate of 10 °C/min. The Brunauer–Emmett–Teller (BET) surface area was measured based on N_2 adsorption–desorption isotherms at 77 K using a Bel Max adsorption volumetric analyzer.

Computational calculation

The calculations reported herein were performed based on spin-polarized DFT within the generalized gradient approximation (GGA), and the model of Perdew, Burke, and Ernzerhof (PBE), as implemented in the Vienna Ab Initio Simulation Package (VASP).[1,2] The projector augmented wave (PAW) method with a plane wave basis set was employed to describe the interaction between the core and valence electrons.[3] An energy cutoff of 400 eV was applied for plane wave expansion of the electronic eigenfunctions. For the Brillouin zone integration, we used a 2 × 2 × 1 Monkhorst-Pack mesh of k points to determine the optimal geometries, and we increased the k-point mesh to 12 × 12 × 1 for the electronic structure calculation. As shown in Fig. S1a, the graphite model used in this study is a hexagonal closed pack (hcp) (0001) surface that consisted of a 4 x 4 hexagonal surface unit cell. Lattice parameter of bulk graphite is a = b= 2.453 Å, c =6.688 Å which is in a good agreement with experimental value (a = b= 2.461 Å, c =6.708 Å) and the dimension of periodic system is 9.813 Å × 9.813 Å × 33.439 Å, including vacuum space of 22.80 Å. Here, four N atoms and one M atom were replaced. For the geometric optimization, the conjugate gradient method was used until residual forces on all the constituent atoms become smaller than 5×10^{-2} eV/Å For the calculation of binding energies of adsorbates (E_{be}) such as O_2, OOH, and H on C@C_3N_4-Pd_1 and C@C_3N_4-Pt_1, we used the following equation.

$$E_{be} = E_{Total} - (E_{clean} + E_{ads}) \quad (3)$$

where E_{Total} is the total energy of the adsorbates being absorbed on M-N-C, E_{clean} is the energy of M-N-C and E_{ads} is the energy of the adsorbates such as O_2, OOH and H.

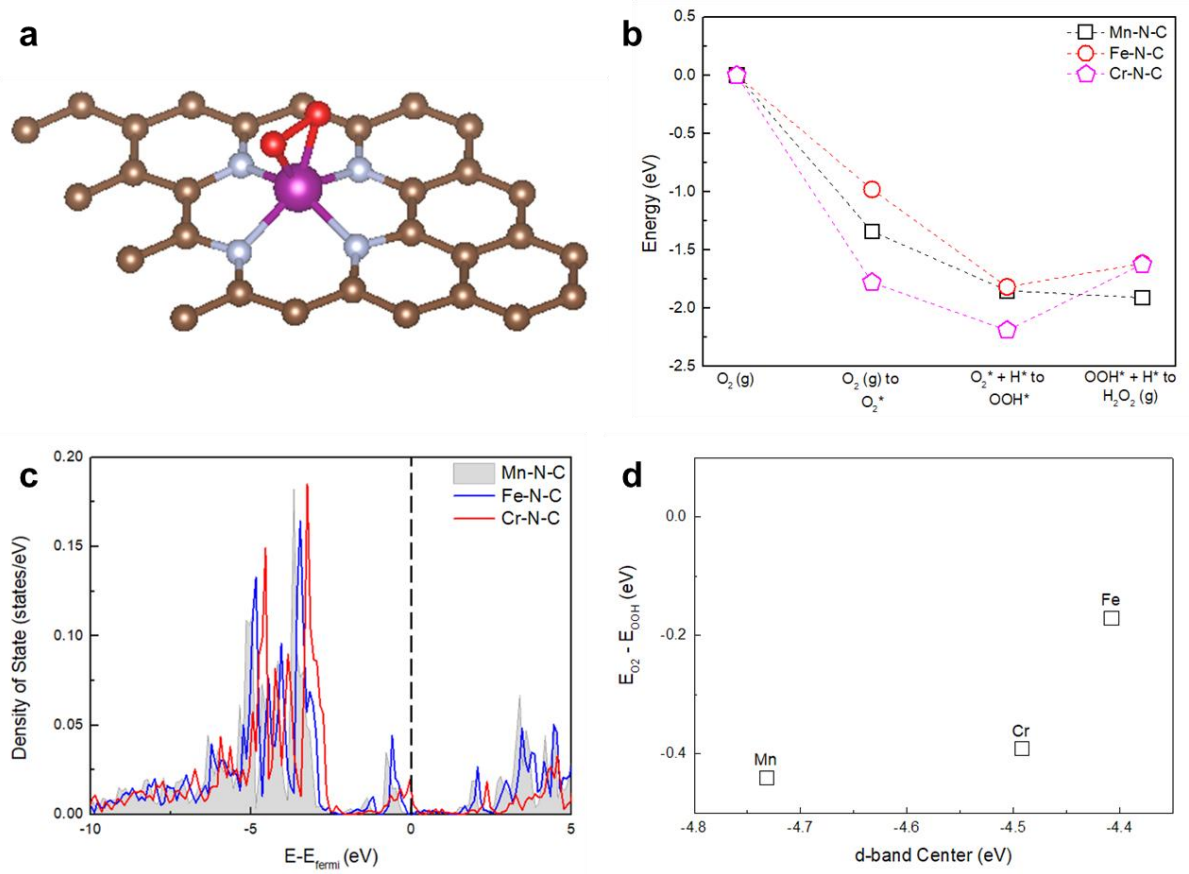

Fig. S1. (a) The visual presentation of the M-N-C catalyst. The brown, blue, purple and red balls represent carbon, nitrogen, metal (Cr, Mn, Fe) and oxygen respectively. (b) Energetics of H_2O_2 synthesis on Mn-N-C, Fe-N-C and Cr-N-C, (c) Density of states of d-band of a Mn, Fe, and Cr atom in M-N-C system (0eV stands for Fermi level), (d) graphical illustration of the relationship between d-band center and EO_2 – EOOH.

In order to propose the catalytic components in carbon composites, we designed three M-N-C catalyst (M: Mn, Fe, and Cr) systems (Fig. S1a) and conducted DFT calculation for binding energies that are required to describe H_2O_2 synthesis reaction pathways. Unlike $4e^-$ pathways of ORR mechanism, which involves a dissociation of O-O bond and leads to the production of H_2O, the chemisorbed O_2 bond is reduced to H_2O_2 via $2e^-$ pathway.[4] For the $2e^-$ pathway, a formation of OOH and H_2O_2 takes place as shown in the following equation.

$$E_{1,}\ O(g) \rightarrow O_2^* \qquad (4)$$

$$E_{2,}\ O_2^* + H^* \rightarrow OOH^* \qquad (5)$$

$$E_{3,}\ OOH + H^* \rightarrow H_2O_2^* \qquad (6)$$

The first step E_1, oxygen affinity, often known as the key intermediate in the ORR, is also responsible for increasing/decreasing H_2O_2 selectivity.[5,6] In the previous studies, strong binding enrgy O_2 facilitates the dissociation of O-O bond, and thus the reduction of O_2 is often hindered.[4] As shown in Fig. S1b, the binding energy of O_2 is the strongest on Cr-N-C (-1.78 eV) and Mn-N-C (-1.34 eV), followed by Fe-N-C (-0.98 eV). Likewise, the reaction energy of $O_2^* + H^* \rightarrow OOH^*$ is the least exothermic on Cr-N-C system with ΔE_2 = -0.41 eV and followed by Mn-N-C with ΔE_2 = -0.51eV whereas ΔE_2 of Fe-N-C exhibits stronger exothermic reaction energies as expected. In H_2O_2 production pathway, the binding energy of OOH is also important since the second reduction step, which is E_3 $OOH^* + H^* \rightarrow H_2O_2$, is reported to be the rate-determing step in the H_2O_2 production pathway. Here, according to our calculation, the order of interaction between M and OOH is the lowest in Mn >> Fe >> Cr, with E_{OOH} is -0.91, -1.02 and -1.39 eV, respectively. Since the binding energy of OOH is lowest in Mn-N-C, the reduction of OOH is expected to be the most exothermic in Mn-N-C as well and the opposite for Cr-N-C. To confirm such prediction, the energetics of $E_{3,}\ OOH + H^* \rightarrow H_2O_2^*$ is further calculated. Mn-N-C exhibits exothermic reaction energy of -0.06 eV whereas the opposite is true for Fe-N-C and Cr-N-C, showing endothermic reaction energy of 0.20 eV and 0.57 eV respectively. Here, OOH in Fe-N-C and Cr-N-C is unlikely to be further reduced to H_2O_2. Our DFT calculation suggests that the catalytic activity in H_2O_2 synthesis on Mn-N-C system is superior than Fe-N-C and Cr-N-C.

To furthur investigate the underlying reason for the enhanced catalytic activity on Mn-N-C, the electronic structures of Mn, Fe, and Cr atoms are considered in M-N-C system by calculating density of d-state. In Fig. S1c, it is clear that the density of Cr and Fe is shifted-up toward the Fermi level in comparison to that of Mn. The density near the fermi level ($-0.25 < E-E_f < 0$), also known as d-band occupancy, is the most dense for Cr, suggesting that the catalytic activity for H_2O_2 production is the lowest, as the previous study demonstrated the relationship between the activity and d-band occupancy near the fermi level.[7] Correpondingly, in the rate-determining step, Cr is revealed to be the most endothermic, and correspondingly the only exothermic Mn exhibits low d-band occupancy near the fermi level. Finally, our calculation results also suggest that the binding energy of E_{O2}-E_{OOH} can be used as a descriptor for H_2O_2 production as increasing/decreasing d-band center result in the stronger/weaker binding energy of E_{O2}-E_{OOH} (Fig. S1d), which is in a good agreement with the d-band center theory.[8]

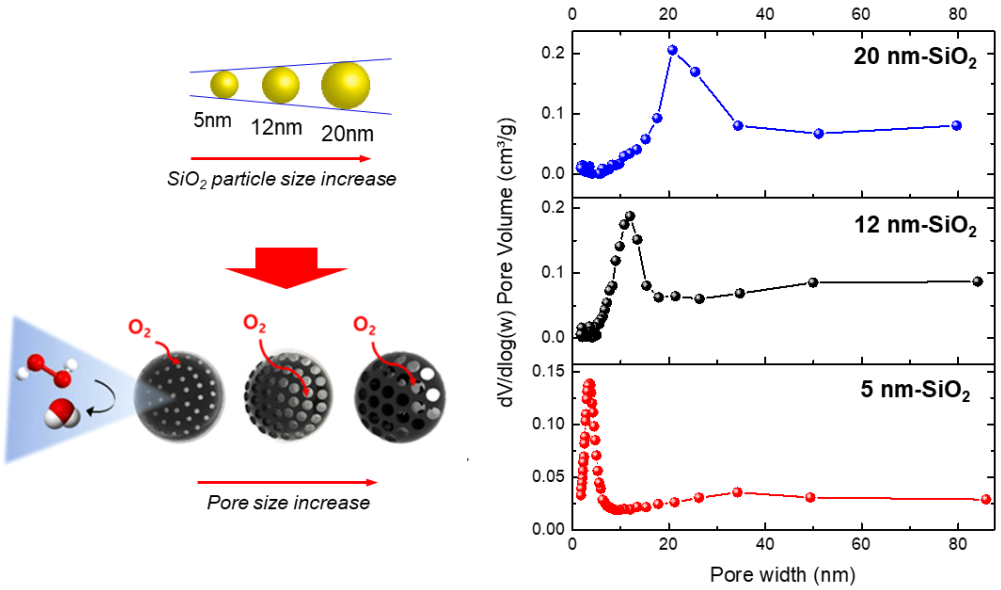

Fig. S2. BET pore size distribution of synthesized carbon with 5, 12, and 20 nm silica particles.

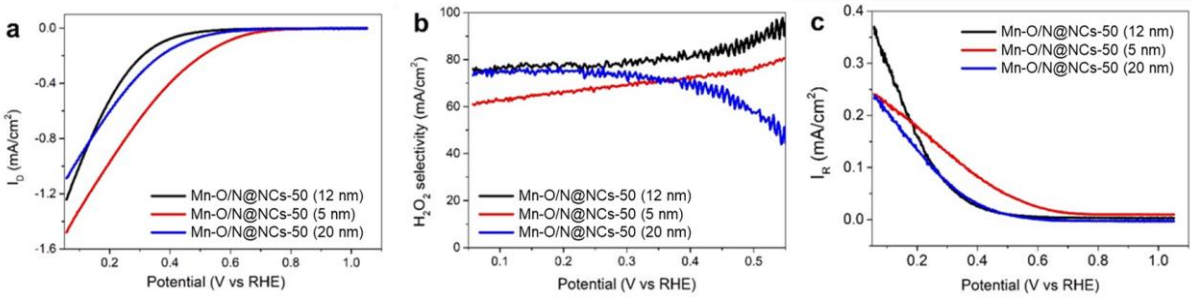

Fig. S3. a) Disk current density, b) H_2O_2 selectivity, and c) ring current density of Mn-O/N@NCs-50 using 5, 12, and 20 nm-sized silica nanoparticles, tested under O_2 purged 0.1 M $HClO_4$ solution at a rotation rate of 900 rpm.

Three sizes of silica particles (5, 12 and 20 nm) were used as a template to assess the effect of carbon pore size on ORR performance. The onset potential for both the 5 and 20 nm samples was higher than that for Mn-O/N@NCs-50 made with 12-nm silica (Fig. S3a). The ORR selectivity toward H_2O_2 was slightly higher for Mn-O/N@NCs-50 (12 nm) than for the other two cases. The presence of micropores in the 5 nm sample may have trapped the resultant H_2O_2 and disproportionation of H_2O_2 ($H_2O_2 \rightarrow H_2O + 1/2O_2$) could have occurred, leading to decreased selectivity toward H_2O_2. The pores of the 20-nm sample were relatively large and the surface area decreased from 43.65 m^2/g (12 nm) to 32.33 m^2/g (20 nm), decreasing the active sites for the ORR. The pore size for generating H_2O_2 is important because it affects the number of exposed active sites and further disproportionation of hydrogen peroxide inside the pores.

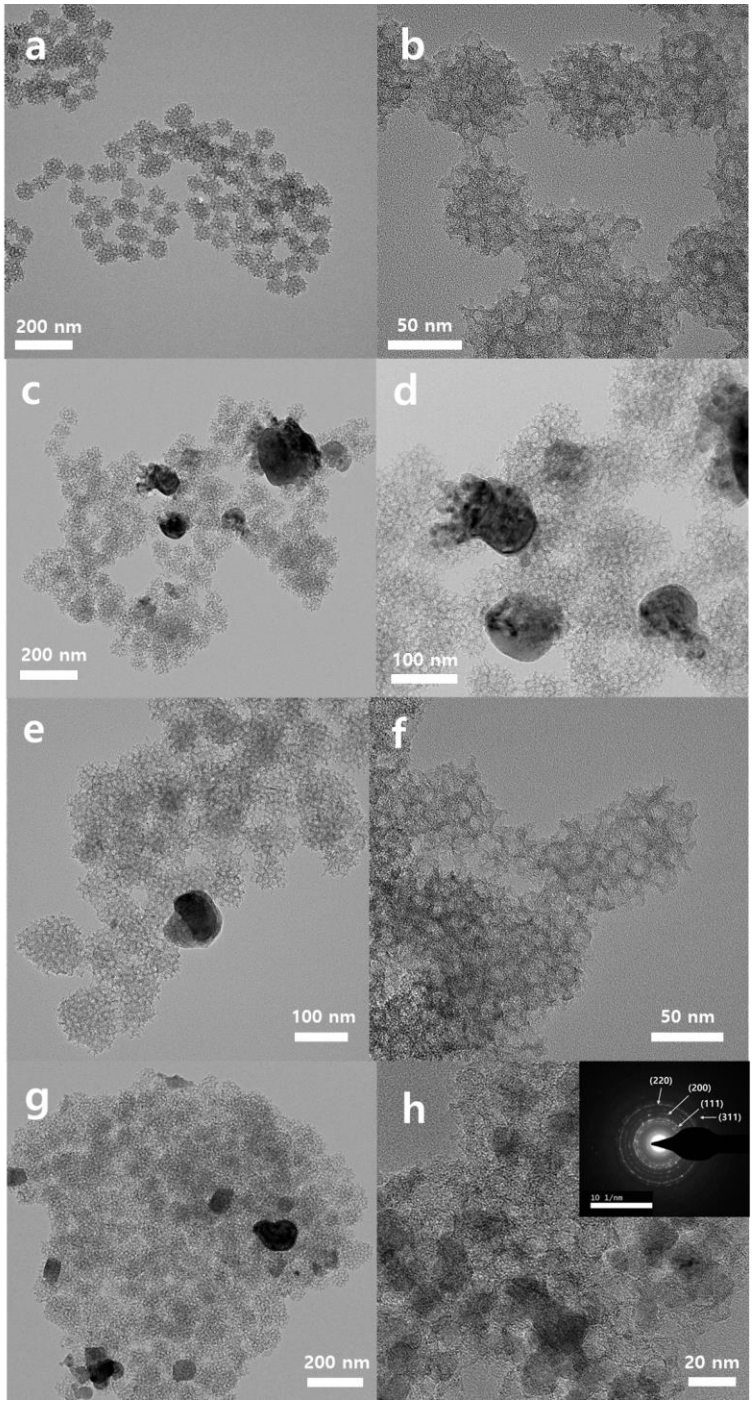

Fig. S4. TEM image of (a, b) NCs, (c, d) Mn-O/N@NCs-5, (e, f) Mn-O/N@NCs-20, and (g, h) Mn-O/N@NCs-50.

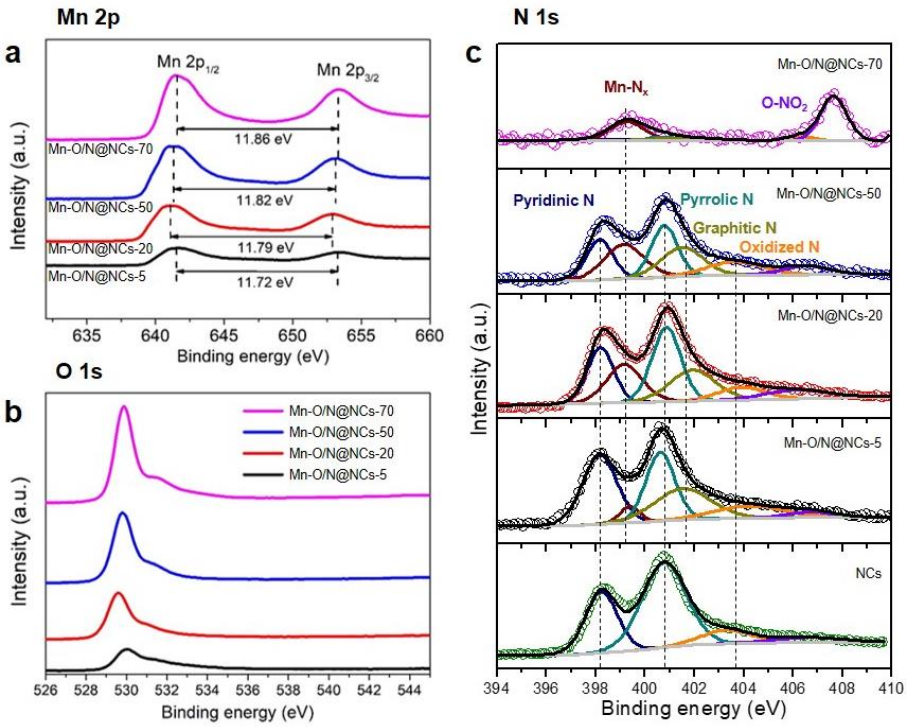

Fig. S5. X-ray photoelectron spectroscopy (XPS) spectra in (a) Mn 2p, (b) O 1s, and (c) N 1s regions for Mn-O/N@NCs-5, Mn-O/N@NCs-20, Mn-O/N@NCs-50, and Mn-O/N@NCs-70.

Table S1. Surface chemical composition of NCs, Mn-O/N@NCs-5, Mn-O/N@NCs-20, Mn-O/N@NCs-50, and Mn-O/N@NCs-70 determined from XPS analysis.

		N 1s						O 1s			Mn 2p					
											Mn^{2+}			Mn^{3+}		Mn^{4+}
		Pyridinic N	Mn-Nx	Pyrrolic N	Graphitic N	Oxidized N	$O-NO_2$	Mn-O	C-O	C-O/carbon *	Mn $2p_{3/2}$	Mn $2p_{1/2}$	satellite	Mn $2p_{3/2}$	Mn $2p_{1/2}$	Mn $2p_{3/2}$
NCs	B.E. (eV)	398.22	-	400.77	401.84	403.31	406.63	-	-	-	-	-	-	-	-	-
	At. ratio (%)	29.14	-	55.38	-	10.28	5.20	-	-	-	-	-	-	-	-	-
Mn-O/N@NCs-5	B.E. (eV)	398.16	399.39	400.62	601.52	404.22	406.73	529.94	531.24	532.80	641.16	645.97	652.84	642.74	654.25	-
	At. ratio (%)	31.55	4.37	26.05	23.09	11.37	3.57	0.48	0.44	0.36	35.71	8.57	19.64	26.79	9.29	-
											63.92			36.08		
Mn-O/N@NCs-20	B.E. (eV)	398.20	399.17	400.86	401.94	403.9	406.17	529.54	530.89	532.33	640.83	652.59	654.96	642.73	654.25	-
	At. ratio (%)	19.24	18.26	28.07	18.90	7.95	7.58	0.77	0.17	0.05	46.08	24.88	4.61	19.82	4.61	-
											75.57			24.43		
Mn-O/N@NCs-50	B.E. (eV)	398.16	399.16	400.78	401.51	403.64	406.52	529.76	531.13	532.38	640.92	652.69	645.75	642.70	654.27	-
	At. ratio (%)	17.76	23.06	22.60	20.32	12.45	3.80	0.79	0.17	0.04	45.87	22.02	5.96	19.72	6.42	-
											73.85			26.14		
Mn-O/N@NCs-70	B.E. (eV)	398.20	399.29	400.67	401.77	406.24	407.64	529.86	531.38	533.16	-	-	-	641.25	653.19	642.76
	At. ratio (%)	4.83	27.80	4.64	9.16	5.37	48.20	0.78	0.17	0.04	-	-	-	43.86	27.63	28.51
														71.49		

Table S2. The H_2O_2 selectivity of previously reported catalysts for the comparison purpose.

No.	Type	Catalyst	H_2O_2 selectivity (potential vs RHE)		Electrolyte	Method	Reference
1	Non-precious carbon-based catalyst	**Mn-O/N@NCs-50**	**74 % at 0.2 V**	**87 % at 0.5 V**	**0.1 M $HClO_4$**	**RRDE**	**This work**
2		Mn-CNT	27 % at 0.2 V		0.1 M KOH	RRDE	Nat. Commun., (2019)[9]
3		Co-CNT	63 % at 0.2 V				
4		CNTs	55 % at 0.2 V		0.1 M KOH	RRDE	Nat. Catal. (2018)[10]
5		O-CNTs	82 % at 0.2 V				
6		F-doped porous carbon	80 % at 0.1 V		0.05 M H_2SO_4	RRDE	J. Catal. (2018)[11]
7		B, N- doped carbon	62 % at 0.2 V		0.1 M KOH	RRDE	J. Am. Chem. Soc. (2018)[12]
8		Mesoporous C	85 % at 0.2 V		0.1 M KOH	RRDE	React. Chem. Eng. (2017)[13]
9		Fe_3O_4/graphene	63 % at 0.2 V		1 M KOH	RRDE	Electrochim. Acta (2015)[14]
10		N-doped AC	58 % at 0.1 V		0.5 M H_2SO_4	RRDE	ACS Catal. (2014)[15]
12		Cobalt-C	94 % at 0.2 V	55 % at 0.6 V	0.1 M $HClO_4$	RRDE	Electrochim. Acta (2011)[16]
13		Cobalt porphyrin-C	50 % at 0.2 V		H_2SO_4 (pH=1)	RRDE	J. Appl. Electrochem. (2006)[17]
14	Precious metal catalyst	Pt-Sulfur doped C	95 % at 0.1 V		0.1 M $HClO_4$	RRDE	Nat. Commun. (2016)[18]
15		Pd-Hg/C	95 % at 0.3 V		0.1 M $HClO_4$	RRDE	Nano Lett. (2014)[19]
16		Pt-Hg/C	96 % at 0.2 V		0.1 M $HClO_4$	RRDE	Nat. Mater. (2013)[20]

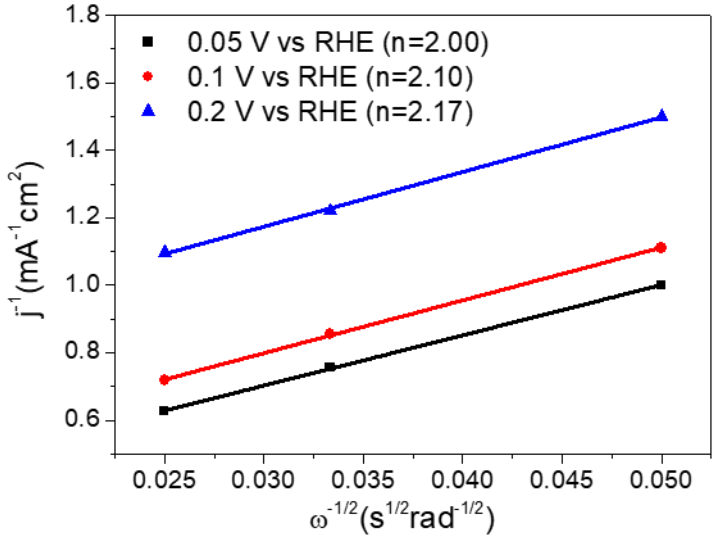

Fig. S6. K-L plots and calculated electron transfer numbers (n) of Mn-O/N@NCs-50. The electrochemical measurements were performed in O_2 purged 0.1 M $HClO_4$ soluation at 400, 900, and 1,600 rpm.

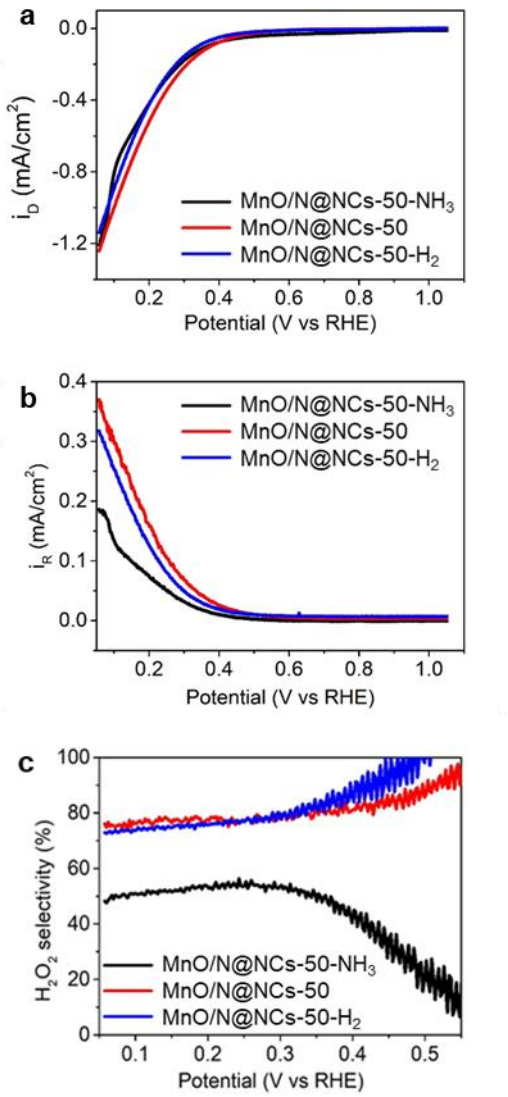

Fig. S7. (a) Disk and (b) ring current densities, and (c) corresponding H_2O_2 selectivity for Mn-O/N@NCs-50, Mn-O/N@NCs-50-NH_3 and Mn-O/N@NCs-50-H_2**.** All electrochemical measurements were performed in O_2 purged 0.1 M $HClO_4$ solution at 900 rpm and ring potential was constant at 1.2 V_{RHE}.

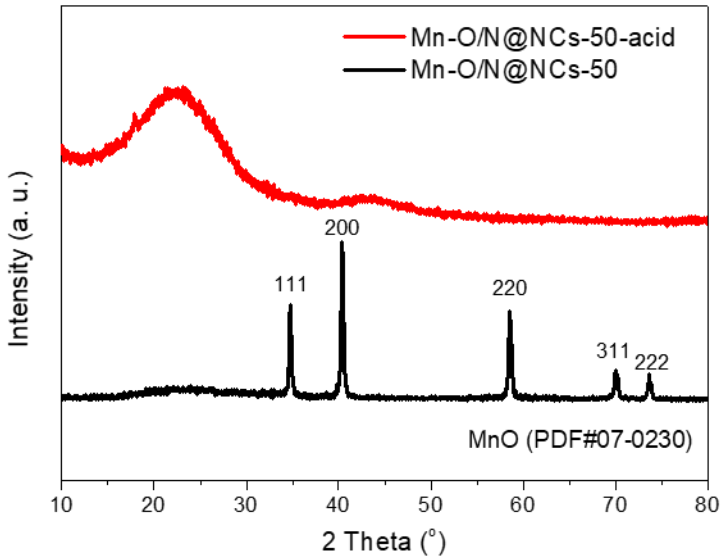

Fig. S8. XRD spectra for Mn-O/N@NCs-50 and Mn-O/N@NCs-50-acid.

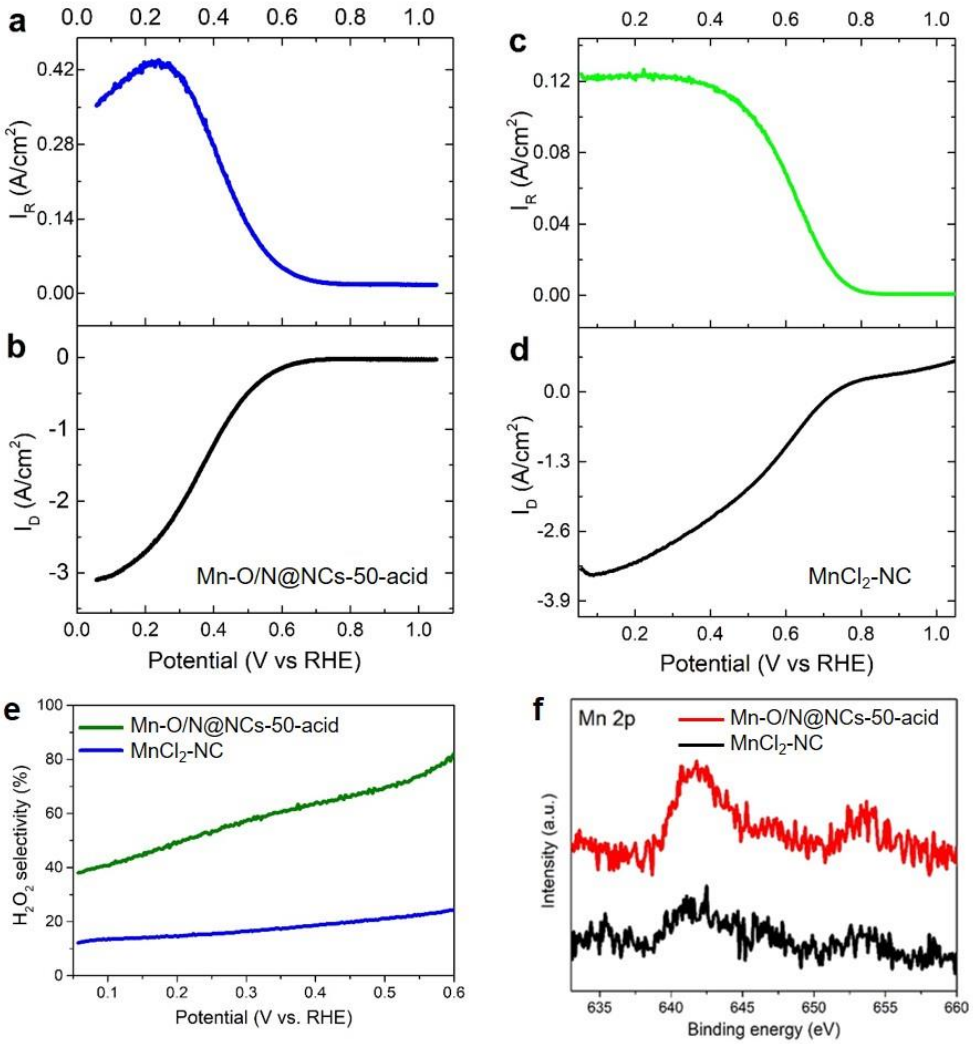

Fig. S9. a) Disk current density, b) ring current density of Mn-O/N@NCs-50-acid, c) disk current density, and d) ring current density of $MnCl_2$-NC, (e) H_2O_2 selectivity, and (f) XPS Mn 2p spectra for Mn-O/N@NCs-50-acid and $MnCl_2$-NC.

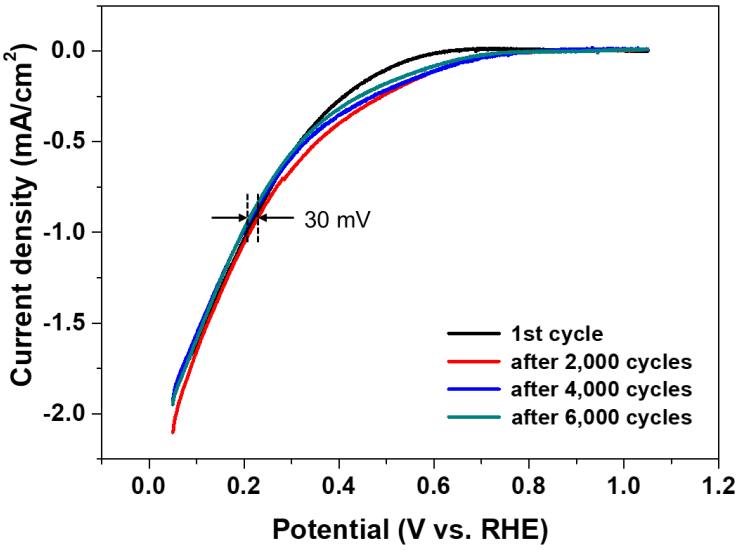

Fig. S10. The polarization curves before and after accelerated degradation test (ADT) cycles (2,000, 4,000 and 6,000 cycles) at the rotating speed of 900 rpm in the potential range from 0.6 to 1.1 V.

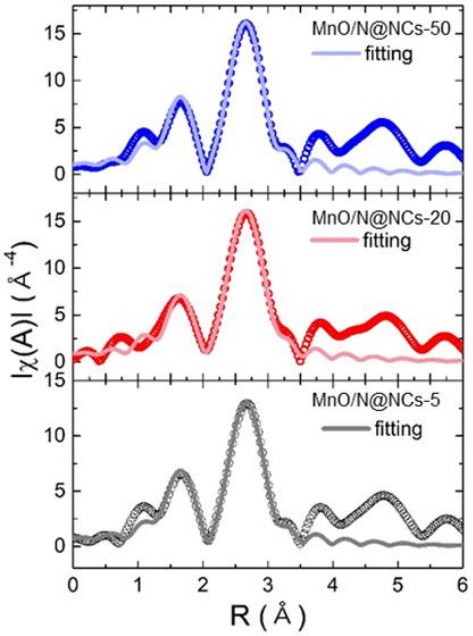

MnO/N@NCs-5	CN	R(Å)	σ^2
Mn-N	6.9	2.25	0.005
Mn-O	4.3	2.46	0.01
Mn-Mn	11.5	3.12	0.01
MnO/N@NCs-20	CN	R(Å)	σ^2
Mn-N	9.5	2.27	2.27
Mn-O	6.1	2.51	2.51
Mn-Mn	12.1	3.12	3.12
MnO/N@NCs-50	CN	R(Å)	σ^2
Mn-N	9.7	2.27	2.27
Mn-O	10.7	2.49	2.49
Mn-Mn	12.3	3.12	3.12

Fig. S11. Fourier Transform of Extended X-ray absorption fine structure spectra (EXAFS) of Mn-O/N@NCs-5, Mn-O/N@NCs-20, and Mn-O/N@NCs-50. Raw data (open circles) are fitted (solid line), and the cooridination number, radial distance and Debye-Waller factor of the materials obtained from EXAFS analysis in the table.

References

1 J. P. Perdew, K. Burke and M. Ernzerhof, *Phys. Rev. Lett.*, 1996, **77**, 3865–3868.

2 G. F. Kresse, *VASP the Guide*, Vienna University of Technology, 2001.

3 P. E. Blöchl, J. Kästner and C. J. Först, in *Handbook of Materials Modeling*, Springer Netherlands, Dordrecht, 2005, pp. 93–119.

4 C. H. Choi, H. C. Kwon, S. Yook, H. Shin, H. Kim and M. Choi, *J. Phys. Chem. C*, 2014, **118**, 30063–30070.

5 J. K. Nørskov, J. Rossmeisl, A. A. Logadottir, L. Lindqvist, J. R. Kitchin, T. Bligaard and H. Jónsson, *J. Phys. Chem. B*, 2004, **108**, 17886–17892.

6 Y. Sha, T. H. Yu, B. V. Merinov, P. Shirvanian and W. A. Goddard, *J. Phys. Chem. Lett.*, 2011, **2**, 572–576.

7 J. Cho, S. Lee, S. P. Yoon, J. Han, S. W. Nam, K.-Y. Lee and H. C. Ham, *ACS Catal.*, 2017, **7**, 2553–2562.

8 J. K. Nørskov, F. Abild-Pedersen, F. Studt and T. Bligaard, *Proc. Natl. Acad. Sci.*, 2011, **108**, 937–943.

9 K. Jiang, S. Back, A. J. Akey, C. Xia, Y. Hu, W. Liang, D. Schaak, E. Stavitski, J. K. Nørskov, S. Siahrostami and H. Wang, *Nat. Commun.*, 2019, **10**, 3997.

10 Z. Lu, G. Chen, S. Siahrostami, Z. Chen, K. Liu, J. Xie, L. Liao, T. Wu, D. Lin, Y. Liu, T. F. Jaramillo, J. K. Nørskov and Y. Cui, *Nat. Catal.*, 2018, **1**, 156–162.

11 K. Zhao, Y. Su, X. Quan, Y. Liu, S. Chen and H. Yu, *J. Catal.*, 2018, **357**, 118–126.

12 S. Chen, Z. Chen, S. Siahrostami, D. Higgins, D. Nordlund, D. Sokaras, T. R. Kim, Y. Liu, X. Yan, E. Nilsson, R. Sinclair, J. K. Nørskov, T. F. Jaramillo and Z. Bao, *J. Am. Chem. Soc.*, 2018, **140**, 7851–7859.

13 S. Chen, Z. Chen, S. Siahrostami, T. R. Kim, D. Nordlund, D. Sokaras, S. Nowak, J. W. F. To, D. Higgins, R. Sinclair, J. K. Nørskov, T. F. Jaramillo and Z. Bao, *ACS Sustain. Chem. Eng.*, 2018, **6**, 311–317.

14 G. Xia, Y. Lu and H. Xu, *Electrochim. Acta*, 2015, **158**, 390–396.

15 J. Park, Y. Nabae, T. Hayakawa and M. Kakimoto, *ACS Catal.*, 2014, **4**, 3749–3754.

16 A. Bonakdarpour, D. Esau, H. Cheng, A. Wang, E. Gyenge and D. P. Wilkinson, *Electrochim. Acta*, 2011, **56**, 9074–9081.

17 N. Guillet, L. Roué, S. Marcotte, D. Villers, J. P. Dodelet, N. Chhim and S. T. Vin, *J. Appl. Electrochem.*, 2006, **36**, 863–870.

18 C. H. Choi, M. Kim, H. C. Kwon, S. J. Cho, S. Yun, H.-T. Kim, K. J. J. Mayrhofer, H. Kim and M. Choi, *Nat. Commun.*, 2016, **7**, 10922.

19 A. Verdaguer-Casadevall, D. Deiana, M. Karamad, S. Siahrostami, P. Malacrida, T. W. Hansen, J. Rossmeisl, I. Chorkendorff and I. E. L. Stephens, *Nano Lett.*, 2014, **14**, 1603–1608.

20 S. Siahrostami, A. Verdaguer-Casadevall, M. Karamad, D. Deiana, P. Malacrida, B. Wickman, M. Escudero-Escribano, E. A. Paoli, R. Frydendal, T. W. Hansen, I. Chorkendorff, I. E. L. S. Stephens, I. E. Stephens and J. Rossmeisl, *Nat. Mater.*, 2013, **12**, 1137–1143.